Frame Vibration Suppression Method
for Sensorless PMSM Drive Applications

Supharat Suthep[†], Yankai Wang[*], Muneaki Ishida[*], Naoki Yamamura[*], Kazuhiro Yubai[*], and Satoshi Komada[*]

[†,*]Dept. of Electrical and Electronic Eng., Mie University, Mie, Japan

Abstract

This study proposes a novel frame anti-vibration controller for position sensorless PMSM drive application. This controller is called specific component reduction controller (SCRC). SCRC can function without an accelerometer and can achieve speed variable control. This study mainly comprises the following phases. First, the position sensorless control method will be provided. Second, the frame vibration model and load torque ripple will be shown. Third, SCRC will be discussed and its stability will be analyzed. Finally, experimental results show that SCRC can achieve speed variable anti-vibration control and compensate target frequency torque ripple.

Key words: PMSM Position Sensorless control, Speed Variable Frame Anti-vibration control, Specific Component Reduction Control

I. INTRODUCTION

In previous studies [1]-[5], several frame anti-vibration methods have been proposed. In [1], [3], [4], frame vibration suppression systems with accelerometer and encoder have been reported. In [5], the researcher has taken the accelerometer out of the system but a torque sensor has been used to detect vibration. In [2], either an accelerometer or encoder has not been applied into the system; however, system stability analysis has not been performed. Thus, the design method for control parameters has not been shown.

To solve the aforementioned problems, the current study proposes a novel frame anti-vibration control method called specific component reduction control (SCRC). A stability analysis is also performed in this study. SCRC has the following features.

1) An extended electromotive force (EEMF) position sensorless control method is used. This way, the encoder is taken out from the permanent magnet synchronous motor (PMSM) field oriented control (FOC) system.

2) In the proposed system, the estimated speed from the EEMF observer has been taken as the input of SCRC. Consequently, an accelerometer is no longer necessary in the entire system.

3) The Fourier transform (FT) has been applied in SCRC. Only one target frequency component, which is the same as the command speed frequency, has been taken into SCRC. The vibration suppression control system is easily stabilized by the adjustment control parameters in SCRC. High-frequency components are not amplified in SCRC because of a lack of positive feedback in the controller.

4) By proper calculation, SCRC can be utilized as a form of repetitive controller based on the position that is not fluctuated. After simplifying the entire system, a linearized system diagram can be obtained. Nyquist analysis is performed using this system diagram to design two important parameters in SCRC. The target frequency harmonics component, which is the same as the command mechanical speed frequency, can be effectively eliminated with SCRC.

5) An experiment is performed in the different constant speed regions, and speed variable control is also achieved with the design of the parameters in SCRC.

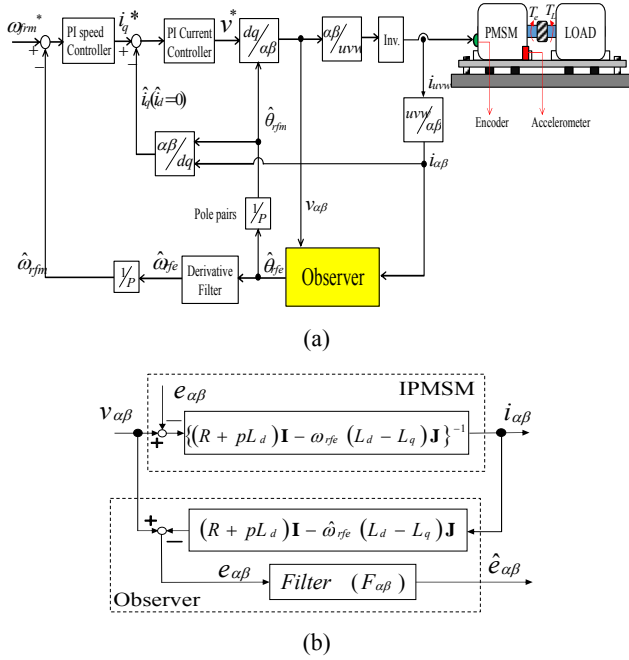These features will be further discussed in the succeeding sections of this paper.

(a)

(b)

Fig. 1. (a) Position sensorless drive system of PMSM. (b) EEMF observer.

II. ESTIMATION OF THE EEMF ALGORITHM

This study utilizes the EEMF observer as a position estimator to construct the position sensorless control system [6]. The voltage equation for the interior PMSM (IPMSM) on the stator frame coordinate (α-β axes) is provided by the following equations:

$$v_{\alpha\beta} = \{(R + pL_d)I - \omega_{rfe}(L_d - L_q)J\}i_{\alpha\beta} + e_{\alpha\beta}. \quad (1)$$

$$e_{\alpha\beta} = \{(L_d - L_q)(\omega_{rfe}i_d - pi_q) + \omega_{rfe}K_e\}J\varepsilon^{J\theta_{rfe}}, \quad (2)$$

where

$$\varepsilon^{J\theta_{rfe}} \equiv \begin{bmatrix} \cos\theta_{rfe} & -\sin\theta_{rfe} \\ \sin\theta_{rfe} & \cos\theta_{rfe} \end{bmatrix}. \quad (3)$$

$$I = \begin{bmatrix} 1 & 0 \\ 0 & 1 \end{bmatrix}, \quad J = \begin{bmatrix} 0 & -1 \\ 1 & 0 \end{bmatrix}. \quad (4)$$

Eq. (2) is defined as EEMF $e_{\alpha\beta} = [e_\alpha \quad e_\beta]^T$. In Eq. (1), v_α and v_β are the voltages on the α-β axes, i_α and i_β are the currents on the α-β axes, R is the stator resistance, L_d and L_q are the inductances on the d-q axes, and p is the differential operator. The estimated motor position $\hat{\theta}_{rfm}$ is obtained by the EEMF observer (see Eq. (7)). The observer includes the filter $F_{\alpha\beta}$ to remove noise caused by modeling errors [6]. The filter characteristics in Fig. 1(b) are provided as follows:

$$\hat{e}_{\alpha\beta} = \alpha I\{(p + \alpha)I - \omega_{rfm}J\}^{-1}e_{\alpha\beta} = F_{\alpha\beta}e_{\alpha\beta}, \quad (5)$$

where

$$F_{\alpha\beta} = \alpha I\{(p + \alpha)I - \omega_{rfe}J\}^{-1}. \quad (6)$$

Moreover, $-\alpha$ is the designed real axis pole of EEMF. The angle estimation is shown as follows
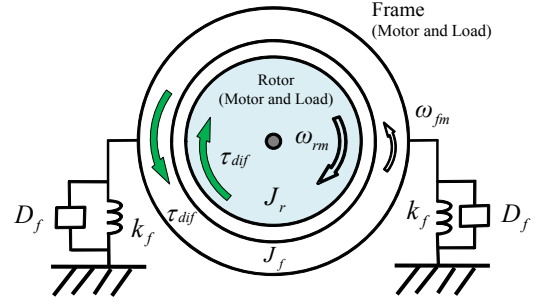

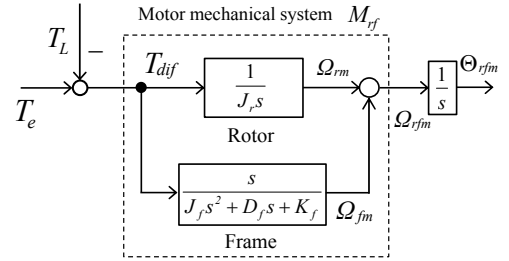Fig. 2. Motor load mechanical model around the motor shaft.

Fig. 3. Block diagram of the motor load mechanical model.

$$\hat{\theta}_{rfm} = \frac{1}{P}\arctan\left(-\frac{\hat{e}_\alpha}{\hat{e}_\beta}\right) = \frac{\hat{\theta}_{rfe}}{P}, \quad (7)$$

where P is the pole number of PMSM. The estimated speed $\hat{\omega}_{rfm}$ is obtained by the derivative filter as follows:

$$\hat{\omega}_{rfm} = \frac{p}{\tau p + 1}\hat{\theta}_{rfm}, \quad (8)$$

where τ is a time constant of the derivative filter.

III. FRAME VIBRATION MODEL AND LOAD TORQUE RIPPLE

A. Motor Load Mechanical Model around the Shaft

Fig. 2 shows the motor load mechanical model (frame vibration model) of the PMSM rotor and frame around the shaft for the typical motor in compressors of air conditioners. In this model, J_r is the rotor inertia; J_f is the frame inertia; D_f and K_f are the frame viscous coefficient and frame spring coefficient, respectively; ω_{rm} is the rotor mechanical speed; ω_{fm} is the frame mechanism speed; θ_{rm} is the rotor mechanical position; and θ_{fm} is the frame mechanical position.

Fig. 3 shows the block diagram of the model shown in Fig. 2, where Ω_{rfm} and Θ_{rfm} are the motor mechanical speed and motor mechanical position, respectively, of the motor frame; T_e is the motor driving torque; T_L is the load torque; and T_{dif} is the total torque.

In general applications, the frame on the stator side is considered standstill. However, the position detected by a position sensor θ_{rfm} in the proposed system includes the error caused by the frame vibration when the torque ripple causes the fluctuation of the frame mechanical speed. Consequently, the motor position θ_{rfm} is described as follows:

$$\theta_{rfm} = \theta_{rm} + \theta_{fm}. \tag{9}$$

B. Load Torque Ripple

In motor drive applications, the causes of torque ripple are categorized as either motor- or load-based. The motor-based factors include cogging torque and spatial harmonics of flux. These factors present a high-frequency torque ripple, such as the 6th harmonics of the motor electrical speed.

Torque ripples based on the load side consist of the load torque ripple $\Delta\tau_{Lrip}$. They present torque ripples with relatively low frequency, such as $1/P$, $2/P$, $3/P$ (P = number of motor pole pair).

This study targets the system in which the motor and load are integrated. In this system, the frame vibration is caused by the load torque ripple $\Delta\tau_{Lrip}$. The mechanical dynamics of the motor frame and rotor in PMSM and load are provided as follows:

$$\Omega_{rfm} = M_{rf}(T_e - T_L) = M_{rf}\ T_{dif}. \tag{10}$$

$$M_{rf}(s) = \frac{(J_r + J_f)s^2 + D_f s + K_f}{J_r s(J_f s^2 + D_f s + K_f)}. \tag{11}$$

$$\tau_L = \tau_{L0} + \Delta\tau_{Lrip}. \tag{12}$$

$$\Delta\tau_{Lrip} = A_{\tau Lrip}\sin(n\theta_{rfm}), \tag{13}$$

where $A_{\tau Lrip}$ is the amplitude of the load torque ripple. The load torque ripple $\Delta\tau_{Lrip}$ is the nth order sinusoidal wave. Accordingly, the periodic speed ripple $\Delta\omega_{rip}$ is expressed as follows:

$$\Delta\omega_{rip} = A_{\omega rip}\sin(n\theta_{rfm} + \varphi_{\omega rip}). \tag{14}$$

IV.　SCRC

The entire speed sensorless anti-vibration control system is shown in Fig. 4. A modified anti-vibration controller called SCRC is proposed in Figs. 5(a) and (b). In SCRC, Fourier coefficients A_n and B_n are extracted by FT and integrated to generate compensation signals A_{n_sum} and B_{n_sum}; k_i is the integration gain and φ_{cn} is the phase compensation gain. SCRC is unlikely to amplify the high-frequency noise of $\hat{\theta}_{rfm}$. Only one target fluctuation frequency component $1/T_r$ is left after FT (see Fig. 5 (b)); thus, the output signal of SG and SG' are shown as follows:

$$i_c' = A_{n\_sum}\cos(\hat{\theta}_{rfm}) + B_{n\_sum}\sin(\hat{\theta}_{rfm}). \tag{15a}$$

$$i_c = A_{n\_sum}\cos(\hat{\theta}_{rfm} + \varphi_{cn}) + B_{n\_sum}\sin(\hat{\theta}_{rfm} + \varphi_{cn}).$$

$$\cong A_{n\_sum}\cos(\frac{2\pi}{T_r}t + \varphi_{cn}) + B_{n\_sum}\sin(\frac{2\pi}{T_r}t + \varphi_{cn}) \tag{15b}$$

where T_r is the cycle time of the rotor mechanical angle, which is constant in a steady state. A_{n_sum} and B_{n_sum} can be calculated as follows:
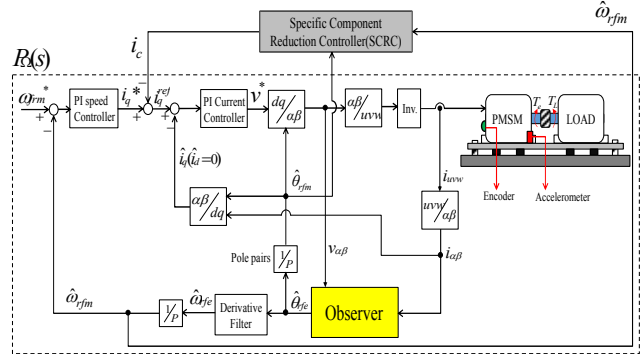

Fig. 4 Proposed position sensorless vibration suppression system with SCRC.

$$A_{n\_sum} = A_{n\_sum}^{(0)} + k_i\int_0^t A_n(t)dt \tag{15c}$$

$$B_{n\_sum} = B_{n\_sum}^{(0)} + k_i\int_0^t B_n(t)dt. $$

Eq. (15c) is considered discrete, which includes the cycle time T_r, and can be expressed as follows:

$$A_{n\_sum}^{(k+1)} = A_{n\_sum}^{(k)} + k_i T_r A_n^{(k)} \tag{15d}$$

$$B_{n\_sum}^{(k+1)} = B_{n\_sum}^{(k)} + k_i T_r B_n^{(k)}.$$

The calculation of the signal after SG in Fig. 5(b) is shown as follows:

$$i_c^{(k+1)} = A_{n\_sum}^{(k+1)}\cos(\frac{2\pi}{T_r}t) + B_{n\_sum}^{(k+1)}\sin(\frac{2\pi}{T_r}t). \tag{15e}$$

$$= A_{n\_sum}^{(k)}\cos(\frac{2\pi}{T_r}t) + B_{n\_sum}^{(k)}\sin(\frac{2\pi}{T_r}t)$$

$$+ k_i T_r\{A_n^{(k+1)}\cos(\frac{2\pi}{T_r}t) + B_n^{(k+1)}\sin(\frac{2\pi}{T_r}t)\}$$

Thus, Eq. (15e) can be expressed as Eq. (15f):

$$i_c^{(k+1)} = i_c^{(k)} + k_i T_r \cdot \Delta\hat{\omega}_{rfm} = i_c^{(k)} + \Delta i_c^{(k)}. \tag{15f}$$

Finally, the compensation signal i_c in Fig. 5(a) is rewritten in discrete form as follows:

$$i_c = A_{n\_sum}^{(k)}\cos\left(\frac{2\pi}{T_r}t + \varphi_{cn}\right) +$$
$$B_{n\_sum}^{(k)}\sin\left(\frac{2\pi}{T_r}t + \varphi_{cn}\right). \tag{15g}$$

From Eq. (15e) to Eq. (15g), SCRC can be established in the form of repetitive controller (see Fig. 5(c)).

Fig. 5(c) shows that SCRC has no influence from the estimated position $\hat{\theta}_{rfm}$, which includes high-frequency noise. This form of SCRC is considered in the system analysis presented in the next section.

Consequently, the stability criterion to determine the compensation gain of k_i and φ_{cn} in SCRC will be discussed
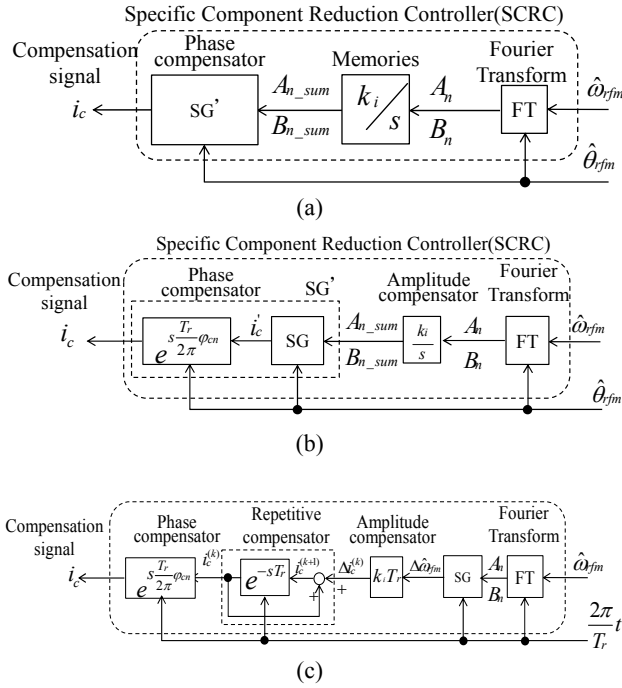
(a)

(b)

(c)

Fig. 5. (a) Original form of SCRC. (b) Equivalent form of SCRC. (c) SCRC in the form of a repetitive controller.

in the next section.

V. STABILITY ANALYSIS OF THE PROPOSED SYSTEM AND DESIGN METHOD FOR THE CONTROL PARAMETERS

A. System Equations and Block Diagrams

To derive the transfer function of $P_\Omega(s)$, we assume that the vibration of θ_{rfe}, ω_{rfe}, $\Delta\theta_{rfe}$, and $\Delta\omega_{rfe}$ (Δ denotes perturbation) are sufficiently small for simplicity, which is satisfied at relatively middle and high speed of over 300 rpm.

Fig. 6 shows the observer in the *d-q* axis (steady state), in which the model in this axis is obtained by transforming Eq. (1) and (2). Using Eq. (16a), the voltage and EMF equations can be taken into the *d-q* axis as follows:

$$\varepsilon^{J\theta_{rfe}} \equiv \begin{bmatrix} \cos\overline{\omega}_{rfe}t & -\sin\overline{\omega}_{rfe}t \\ \sin\overline{\omega}_{rfe}t & \cos\overline{\omega}_{rfe}t \end{bmatrix}. \qquad (16a)$$

$$v_{dq} = \{(R+pL_d)I - \Delta\omega_{rfe}(L_d - L_q)J\}i_{dq} + e_{dq}. \qquad (16b)$$

$$e_{dq} = \{(L_d - L_q)(\omega_{rfe}i_d - pi_q) + \omega_{rfe}K_e\}J\varepsilon^{J(\delta\theta_{rfe})}.$$

$$v_{dq} = \{(R+pL_d)I - \Delta\hat{\omega}_{rfe}(L_d - L_q)J\}i_{dq} + e'_{dq}. \qquad (16c)$$

From Eq. (16b) and Eq. (16c), the flowing equation is derived as follows:

$$e'_{dq} = (\Delta\hat{\omega}_{rfe} - \Delta\omega_{rfe})(L_d - L_q)Ji_{dq} + e_{dq}, \qquad (16d)$$

where $\delta\theta_{rfe} = \theta_{rfe} - \overline{\omega}_{rfe}t$, $\overline{\omega}_{rfe}$ is the speed average of ω_{rfe}, $\overline{\omega}_{rfe} = \frac{1}{T_r}\int_{ta}^{ta+T_r}\omega_{rfe}dt$, t_a is arbitrary time in one period T_r, and $\overline{\theta}_{rfe} = \overline{\omega}_{rfe}t$.
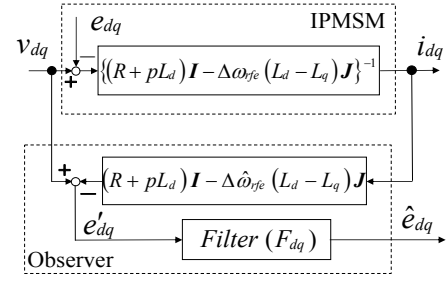

Fig. 6. Observer for estimating the d-q axis component of EEMF.

In Eq. (16d), $\Delta\hat{\omega}_{rfe}$ includes high-frequency noise caused by the imperfection of the motor model; thus, e'_{dq} will not be equal to e_{dq} and the filter F_{dq} is applied to the observer. Consequently, the high-frequency noise of $\Delta\hat{\omega}_{rfe}$ will be reduced; hence, $e'_{dq} \cong e_{dq}$.

The position error is given as follows:

$$\delta\theta_{rfe} = \arctan\left(-\frac{e_d}{e_q}\right) = \arctan\left(-\xi\right). \qquad (17a)$$

$$\Delta(\delta\theta_{rfe}) = \left(\arctan\left(-\xi\right)\right)'\Delta\xi = \frac{1}{1+\xi^2}\Delta\xi;$$

$$\Delta\xi = \frac{e_q \circ \Delta e_d - e_d \circ \Delta e_q}{e_{qo}^2}. \qquad (17b)$$

$$= \frac{e_q \circ \Delta e_d - e_d \circ \Delta e_q}{e_{do}^2 + e_{qo}^2} = K_d\Delta e_d - K_q\Delta e_q.$$

In the same manner,

$$\Delta(\delta\hat{\theta}_{rfe}) = \frac{\hat{e}_{qo}\Delta\hat{e}_d - \hat{e}_d \circ \Delta\hat{e}_q}{\hat{e}_{do}^2 + \hat{e}_{qo}^2} = \hat{K}_d\Delta\hat{e}_d - \hat{K}_q\Delta\hat{e}_q, \quad (17c)$$

where θ_{rfe} and $\hat{\theta}_{rfe}$ are the real and estimated positions, respectively, by providing the perturbation.

Assuming that at the steady state operation point estimated on the *d-q axis* coincides with the real *d-q axis*, Eq. (18a) can be obtained. Thus, Eq. (18b) can be provided.

$$\hat{e}_{do} = e_{do}, \hat{e}_{qo} = e_{qo}. \qquad (18a)$$

$$\hat{K}_d = K_d, \hat{K}_q = K_q. \qquad (18b)$$

The estimated back EMF on the *d-q* (steady state) axes is provided by the following equation:

$$\begin{bmatrix} \hat{e}_d \\ \hat{e}_q \end{bmatrix} = I\hat{e}_{dq} = \frac{\alpha}{(p+\alpha)}Ie_{dq} = \frac{\alpha}{(p+\alpha)}\begin{bmatrix} e_d \\ e_q \end{bmatrix}$$

$$= F_{dq}\begin{bmatrix} e_d \\ e_q \end{bmatrix}. \qquad (19a)$$

$$F_{dq} = \frac{\alpha}{p+\alpha}. \qquad (19b)$$

Eq. (20) is derived by giving perturbation to Eq. (19a).

$$\begin{bmatrix} \Delta\hat{e}_d \\ \Delta\hat{e}_q \end{bmatrix} = \frac{\alpha}{p+\alpha}\begin{bmatrix} \Delta e'_d \\ \Delta e'_q \end{bmatrix} \cong \frac{\alpha}{p+\alpha}\begin{bmatrix} \Delta e_d \\ \Delta e_q \end{bmatrix}. \qquad (20)$$

From Eqs. (17b), (17c), (18a), (18b), and (20), the relationship between real and estimated positions is provided as follows:

$$\frac{\Delta(\delta\hat\theta_{rfe})}{\Delta(\delta\theta_{rfe})} = \frac{P*\Delta(\delta\hat\theta_{rfm})}{P*\Delta(\delta\theta_{rfm})} = \frac{\alpha}{p+\alpha}. \quad (21a)$$

Considering Eq. (8),

$$\frac{\Delta\hat\Omega_{rfe}}{\Delta\hat\Omega_{rfe}} = \frac{P*\Delta(\delta\hat\theta_{rfm})}{P*\Delta(\delta\theta_{rfm})} = \frac{\alpha}{p+\alpha}. \quad (21b)$$

Assuming that the position angle error $\delta\theta_{rfm} = \hat\theta_{rfm} - \theta_{rfm}$ is sufficiently small ($cos\delta\theta_{rfm} \cong 1$), the current controller on the $\hat d$-$\hat q$ axes is considered an ideal state because the current controller loop gain is high enough when SCRC is operated in the relatively low frequency region. Moreover, $\hat i_d = 0$ and the motor torque T_e is given as Eq. (22), where $\hat i_q$ is the current on the estimated q-axes calculated by $\hat\theta_{rfm}$. Accordingly, the relationship between the real and estimated speeds is provided as the first-order low-pass filter shown in Eq. (19b).

$$T_e = PK_{ef}i_q = PK_e\hat i_q \cos \delta\theta_{rfm} \cong PK_e\hat i_q \cong PK_e i_q^{ref} \quad (22)$$

Using Eq. (22), the system shown in Fig. 7 is obtained by considering Eqs. (11) and (21.2) with respect to the perturbed variables (ΔI_{dq}, $\Delta\Omega_{rfm}$, and $\Delta\hat\Omega_{rfm}$) around the steady state operating points (I_{dq0}, Ω_{rfm0}, and $\hat\Omega_{rfm0}$), $\Delta T_e = \mathcal{L}\{\Delta\tau_e\}$. In Fig. 7, the transformation $G_1(s)$, $G_2(s)$, $G_3(s)$ and $G_4(s)$ are provided as follows:

$$G_1(s) = \frac{\Delta T_e}{\Delta\hat I_q^{ref}} = PK_e. \quad (23)$$

$$G_2(s) = \frac{\Delta\Omega_{rfm}}{\Delta T_{dif}} = \frac{(J_f + J_r)s^2 + D_f s + K_f}{J_r s(J_f s^2 + D_f s + K_f)}. \quad (24)$$

$$G_3(s) = \frac{\Delta\hat\Omega_{rfm}}{\Delta\hat\Omega_{rfm}} = \frac{\alpha}{s+\alpha}. \quad (25)$$

$$G_4(s) = \frac{\Delta I_q^{ref}}{\Delta\hat\Omega_{rfm}} = -\frac{K_{ps}s + K_{is}}{s}. \quad (26)$$

$$P_\Omega(s) = \frac{\Delta\hat\Omega_{rfm}}{\Delta I_c} \quad (27)$$
$$= [1 + G_1(s)G_2(s)G_3(s)G_4(s)]^{-1} G_1(s)G_2(s)G_3(s).$$

where $G_1(s)$ is the torque equation provided by Eq. (22), $G_2(s)$ is the motor mechanics from Eq. (11), $G_3(s)$ is the filter in the observer derived from Eq. (21b), and $G_4(s)$ is the PI speed controller. ΔI_c is generated by the repetitive controller to suppress the estimated speed ripple in $\Delta\hat\Omega_{rfm}$ which is estimated by the speed estimator. The load torque ΔT_L is a disturbance torque caused by the load torque ripple.

When τ of the derivative filter in Eq. (8) has been selected properly, it can be ignored in the vibration suppression
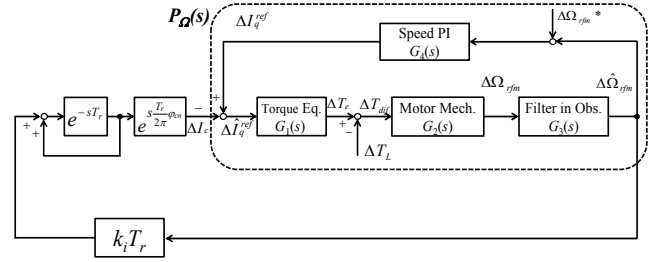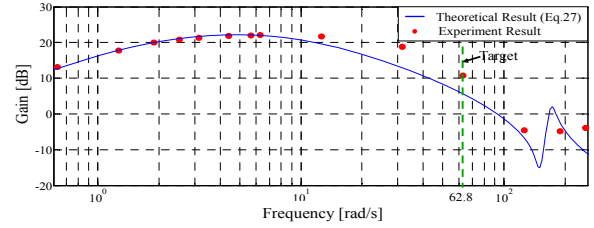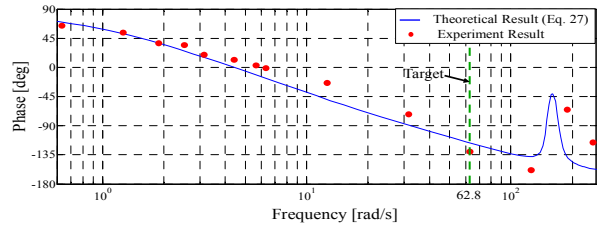

Fig. 7. Proposed system diagram of the linear approximation vibration suppression system.

(a) Bode plot of gain [dB].

(b) Bode plot of phase [deg].

Fig. 8. Bode plots of the transfer function PΩ(s).

system.

The characteristics of $P_\Omega(s)$ in Fig. 7 can be proven by Fig. 8. Fig. 8 shows that the theoretical result has been simulated in Matlab 2014a, and the points are the experimental results of $P_\Omega(s)$ (see Table I and Table II). These results are nearly the same. In our system, τ is 0.2.

B. System Stability

The characteristics of $P_\Omega(s)$ in Fig. 8 show that $P_\Omega(s)$ decreases high-frequency harmonics or noise; thus, the FT extracts only one target 10 Hz into SCRC. Consequently, SCRC will not amplify high-frequency noise or harmonics. However, the proposed system does not amplify high-frequency harmonics or noise. This way, the concept of system analysis shown in [1], [3], [8], [9] can be considered in the stability analysis of the proposed system.

With the input signal $\Delta\hat\Omega_{rfm}$, the block diagram shown in Fig. 7 is transformed into the one shown in Fig. 9. Using small gain theory [3] and [7]-[9], Eq. (27) can be obtained as follows:

$$|1 - C(j\omega_n)P_\Omega(j\omega_n)| < 1. \quad (28)$$

The transfer functions in Fig. 9 are shown as follows:

$$C(s) = k_i T_r e^{s\frac{T_r}{2\pi}\varphi_{cn}}. \quad (29)$$

TABLE I
MOTOR PARAMETERS

IPMSM (Test Bench)		
Rated power	[W]	750
Rated speed	[rpm]	1750
Rated current	[A]	3.5
Number of pole pairs	P_S	3
Stator Resistance	R [Ohm]	1.25
d-axis inductance	L_d [H]	0.0168
q-axis inductance	L_q [H]	0.0218
EMF constant	K_e [V·s/rad]	0.255
Motor inertia	J_r [kg·m^2]	0.0055
Frame inertia	J_f [$kg \cdot m^2$]	0.0207
Frame viscous coefficient	D_f [$kg \cdot m^2/s$]	0.108
Frame rubber coefficient	K_f [N/mm]	148.54
Servo motor (Load Motor)		
Rated power	[W]	850
Rated speed	[rpm]	1500
Rated current	[A]	6.9

TABLE II
EXPERIMENTAL PARAMETERS

Inverter		
DC-link voltage	[V]	200
Carrier frequency	[kHz]	10
Controller		
Control period	[μs]	100
Fourier sampling period	[μs]	1300
Speed command	$\omega_{rfm}*$ [rpm]	600,1200
Speed controller Proportional gain	k_{ps} [A·s/rad]	0.08
Speed controller Integral gain	k_{is} [A/rad]	0.14
Current controller cutoff frequency	[rad/s]	5000
SCRC integration gain	k_3	-5.0, -9.6
SCRC phase gain	k_4	1.8, 2.2
Pole of disturbance observer	α [rad/s]	$0.5\omega_{rfe}$
	β [rad/s]	ω_{rfe}
Load torque	T_L [Nm]	$2.0 + 2.0\sin\theta_{rfm}$

$$G(s) = \frac{\Delta\hat{\Omega}_{rfm}}{\Delta T_L} = G_2(s)G_3(s), \qquad (30)$$

where $P_\Omega(s)$: transfer function of motor and the torque ΔI_c to $\Delta\hat{\Omega}_{rfm}$.

$C(s)$: transfer function of proportional compensator and time leading element.

$G(s)$: transfer function from ΔT_L to $\Delta\hat{\Omega}_{rfm}$.

C. SCRC Parameters k_i, φ_{cn}

Fig. 10 shows the Nyquist plot of $1-C(j\omega_n) P_\Omega(j\omega_n)$. Nyquist analysis is considered according to the criteria expressed in Eq. (28). The operation point A'' remains out of the unit circle, that is, SCRC will be unstable at this point. Thereafter, an operating point can be moved into the unit circle by reversing the sign of k_i shown in Fig. 10(a) (A''→A). Reversing the sign of k_i means a phase shift by π. However, B'' (Fig. 10(b)) cannot be moved into the unit circle by reversing k_i. In such a case, the operation point can be
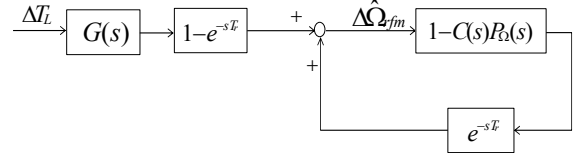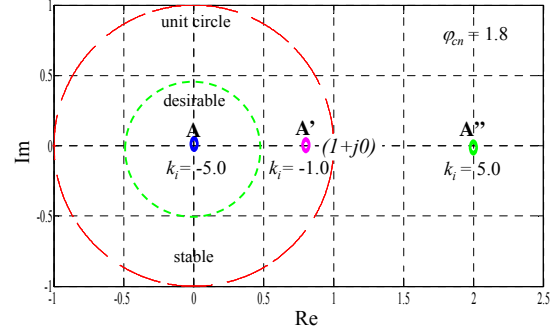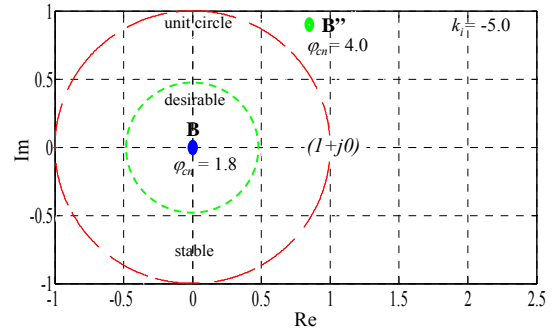

Fig. 9. Transformed equivalent block diagram.

(a) Case A: Operating point exits outside of the unit circle (φ_{cn} = 1.8), and reverse signs of k_i.

(b) Case B: Operating point exits outside of the unit circle with the phase control sign of φ_{cn}.

Fig. 10. Nyquist plot of the transfer function $(1-C(s) P_\Omega(s))$.

moved into the unit circle by using the phase compensator gain φ_{cn} (B''→B).

To place Nyquist point near the original point (i.e., vibration convergence of SCRC is rapid), Eq. (31) is shown as follows:

$$H(j\omega_n) = 1 - C(j\omega_n)P_\Omega(j\omega_n) < 1, \qquad (31)$$

where $H(j\omega_n) \cong 0$; hence,

$$C(j\omega_n) \cong \frac{1}{P_\Omega(j\omega_n)}. \qquad (32)$$

$$P_\Omega(j\omega_n) = A_\Omega e^{(j\varphi_\Omega)} \qquad (33)$$

Using Eqs. (32) and (33), k_i and φ_{cn} can be obtained as follows:

$$\begin{cases} k_i = \dfrac{1}{A_\Omega T_r} \\ \varphi_{cn} = -\varphi_\Omega \end{cases} or \begin{cases} k_i = -\dfrac{1}{A_\Omega T_r} \\ \varphi_{cn} = -\varphi_\Omega \pm \pi \end{cases}. \qquad (34)$$

Therefore, the operation point can be moved within the unit
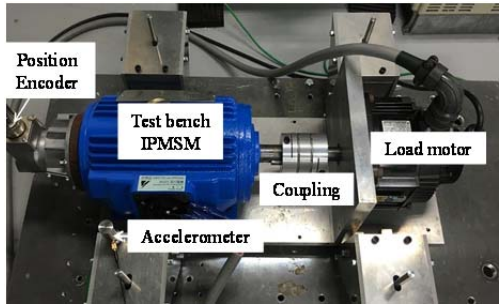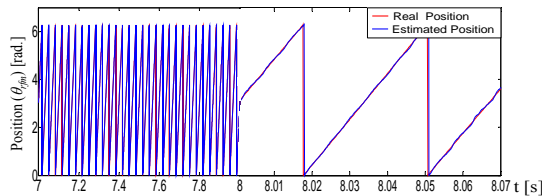
Fig. 11. Overall experiment system.

Fig. 12. Case A: Estimated position $\hat{\theta}_{rfm}$ and real position θ_{rfm}.

circle by adjusting the gain of k_i *and* φ_{cn}. Thus, the control system will be stable.

The EEMF position sensorless system loses stability in the relatively low speed region. In the experimental system, the speed is fluctuated if the load torque is not constant. The low speed region is defined as speed below 300 [rpm]. Experiments have been performed above the base speed of 600 [rpm]. In the proposed system, the speed command of 600 rpm and 1200 rpm have been tested to prove the stability of SCRC.

VI. EXPERIMENT

A. Experimental Setup

The proposed SCRC has been implemented in DSP (TMS320C6713) of Myway Corporation. An experimental setup is depicted in Fig. 11. TABLES I and II show the experimental parameters.

The experiment is performed with the speed command $\omega_{rfm}{}^*$ = 600 rpm, 1200 rpm and $\omega_{rfm}{}^*$ = 600 rpm to 900 rpm, with the load torque $T_L = 2.0 + 2.0\sin\theta_{rfm}$ N. The load torque T_L is generated by a servo motor. At 1 s, the anti-vibration control starts to suppress the torque ripple T_{Lrip}.

B. Experimental Results

Fig. 12 shows the position estimation result and real position. This figure shows that the speed sensorless control system estimation with SCRC runs smoothly.

Figs. 13 to 16 show the three situations in Fig. 10(a). When the Nyquist point is near the original point (Case A), the speed vibration suppression is rapid in Fig. 13(a). When the Nyquist point is in the unit circle but distant from the original point (Case A'), the speed vibration suppression takes considerable time in Fig. 13(b). The target frequency is 94% reduced by SCRC (see Fig. 14). Fig. 15 shows the phase
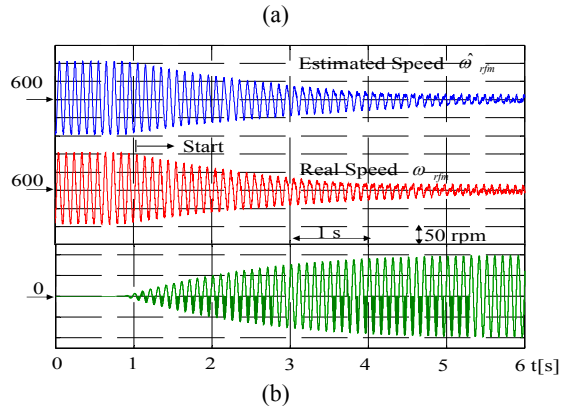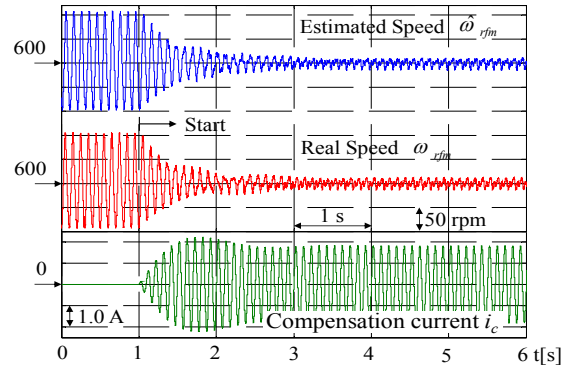

(a)

(b)

Fig. 13. (a) Case A: Rotor speed and compensation current (f = 10 Hz). (b) Case A': Rotor speed and compensation current (f = 10 Hz).

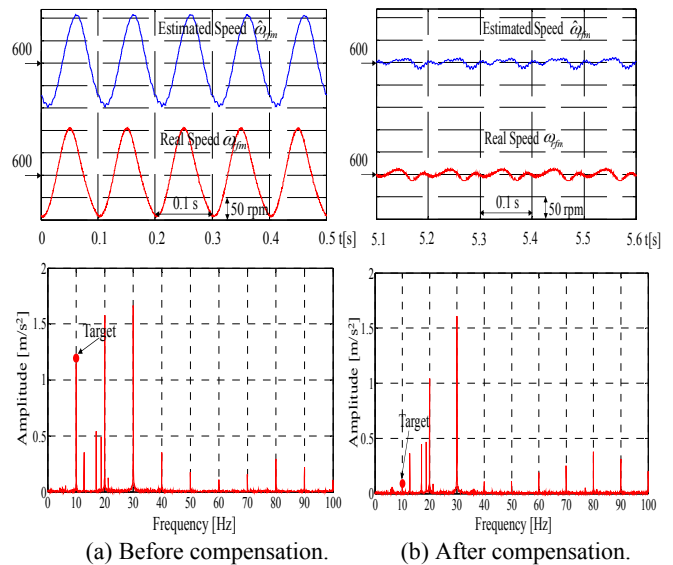(a) Before compensation.   (b) After compensation.

Fig. 14. Enlarged view and FFT of Fig. 13 (a) (f = 10 Hz).

current waveform when the vibration suppression control works (Case A). If the Nyquist point is out of the unit circle (Case A''), then the speed vibration suppression is out of work.

In the same manner, the speed vibration suppression control of 1200 rpm can be achieved; $k_i = -9.6$ and $\varphi_{cn} = 2.2$. Figs. 17 and 18 show that in the speed region of 1200 rpm (20 Hz), the target frequency harmonic (f = 20 Hz component)

(a)   Phase current.

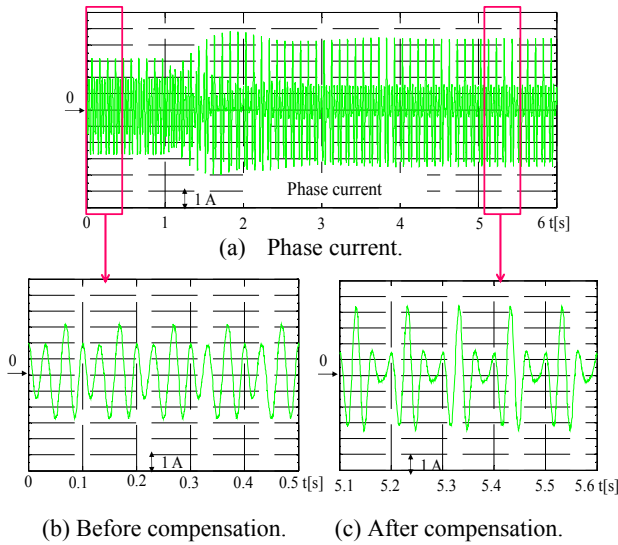(b) Before compensation.   (c) After compensation.

Fig. 15. Phase current and enlarged view of Fig. 13 (a) ($f = 10$ Hz).
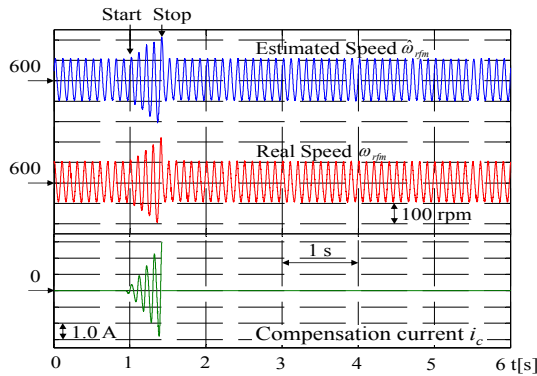
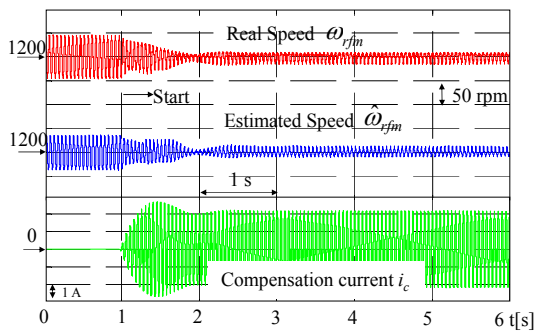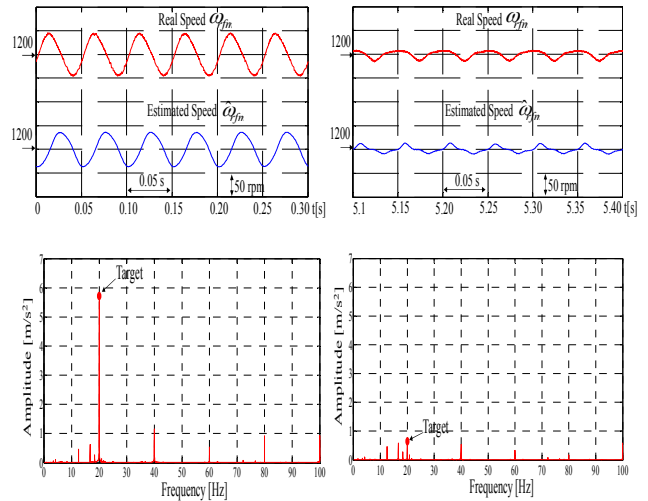Fig. 16. Case A'': Rotor speed and compensation current ($f = 10$ Hz).

Fig. 17. Rotor speed ($f = 20$ Hz).

(a) Before compensation.   (b) After compensation.

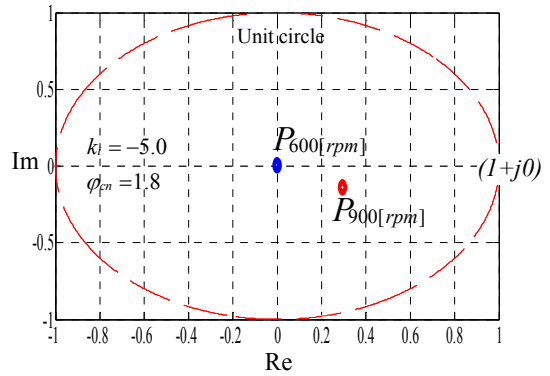Fig. 18. Enlarged view and FFT of Fig. 17 ($f = 20$ Hz).

Fig. 19. Nyquist plot of the transfer function ($1-C(s)\,P_\Omega(s)$).
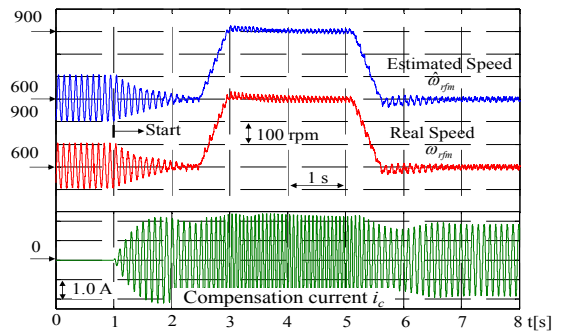
Fig. 20. Speed variable anti-vibration control without encoder and accelerometer.

is reduced by SCRC by approximately 92%. That is, SCRC can work in different speed regions.

If the design of k_i and φ_{cn} makes the Nyquist point of the entire system in the unit circle, then SCRC may achieve sensorless variable speed anti-vibration control without accelerometer.

Fig. 19 shows the Nyquest plot for the variable speed operation under the condition shown in Fig. 10(a) (case A). Figs. 20 to 21 show that SCRC has the ability to achieve variable speed anti-vibration control if the Nyquist analysis is in the unit circle. The target harmonic (step operation $f = 10$ Hz to 15 Hz component) is reduced by SCRC by approximately 94%.
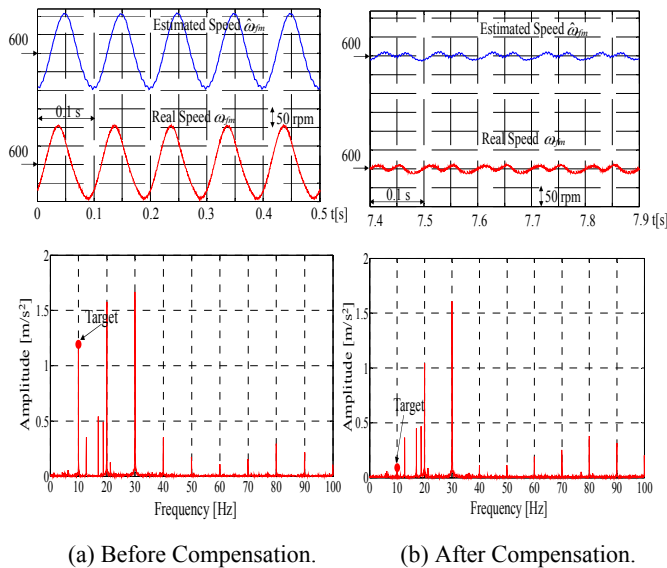
(a) Before Compensation.   (b) After Compensation.

Fig. 21. Enlarged view and FFT of Fig. 20(f = 10 Hz to 15 Hz).

VII. CONCLUSIONS

This paper proposed a novel vibration suppression method called SCRC, which function without accelerometer in the IPMSM position sensorless control system. The EEMF position sensorless control method has been considered. System stability analysis with Nyquist diagram has been proposed to design two important parameters (i.e., k_i and φ_{cn}) in SCRC. The entire system is stable when the Nyquist point with k_i and φ_{cn} in SCRC is within the unit circle. The target frequency harmonics component, which has the same frequency as the command mechanical speed, is eliminated by SCRC as well. The experimental results show that the proposed SCRC with IPMSM position sensorless control system is beneficial for suppressing periodic load torque in different speed regions without accelerometer. The speed variable sensorless anti-vibration control can also be achieved with SCRC.

Our future study will focus on the stability analysis in different speed regions, particularly in the low-speed region. Harmonics frequency components, which are different from the mechanical speed command frequency, will also be considered.

REFERENCES

[1] T. Su, S. Hattori, M. Ishida, and T. Hori, "Suppression control method for torque vibration of ac motor utilizing repetitive controller with Fourier transform," *IEEE Trans. Ind. Appl.*, Vol. 38, No. 5, pp. 1316-1325, Sep. 2002.

[2] M. Zhang, Y. Li, T. Zhao, Z. Liu, and L. Huang, "A speed fluctuation reduction method for sensorless PMSM-compressor system," in *Industrial Electronics Society, 2005. IECON 2005. 31st Annual Conference of IEEE* , pp. 5, 2005.

[3] A. Shimada, K. Kawai, T. Zanma, S. Doki, and M. Ishida, "Sensorless suppression control for frame vibration of PMSM," *IEEJ Trans.*, Vol. 128, No. 11, pp. 1246-1253, 2008.

[4] J. Kim and K. Nam, "Speed ripple reduction of PMSM with eccentric load using sinusoidal compensation method," in *Power Electronics and ECCE Asia (ICPE & ECCE), 2011 IEEE 8th International Conference on*, pp. 1655-1659, 2011.

[5] T. Yamaguchi, Y. Tadano, and N. Hoshi, "Torque ripple suppression control by periodic disturbance observer with model error correction," *IEEJ Trans.*, Vol. 134, No. 2, pp.185-192, 2014.

[6] Z. Chen, M. Tomita, S. Doki, and S. Okuma, "An extended electromotive force model for sensorless control of interior permanent magnet synchronous motors," *IEEE Trans. Ind. Electron.*, Vol. 50, No. 2, pp. 288-295, Apr. 2003.

[7] S. Hattori, M. lshida, and T. Hori, "Suppression control method for torque vibration of brushless DC motor utilizing repetitive control with Fourier transform," in *Proc. 6th International Workshop on Advanced Motion Control*, pp. 427-432, 2000.

[8] M. lshida, T. Su, S. Hattori, and T. Hori, "Suppression control method for torque vibration of AC motor utilizing repetitive controller with Fourier transformer," *Industry Applications Conference of IEEE*, Vol. 3, pp.1675-1682, 2000.

[9] D. S. Naidu, Optimal Control System, Idaho State University Pocatello, Idaho, UAS, 1940.

Suthep Supharat was born in Thailand in 1981. He obtained a BE and ME in Electrical and Industrial Engineering from King Mongkut's University of Technology North Bangkok (2004) and Chiang Mai University (2012), respectively, in Thailand. He has been a PhD candidate in Mie University since 2013. His research interests include the control of electrical drives, particularly frame anti-vibration suppression control for sensorless PMSM driven.

Yankai Wang was born in Shanghai, China in 1992. He obtained a BS in Electrical Engineering from Shanghai Ocean University, Shanghai, China in 2015. He is currently working toward an MS in the Electrical and Electronic Engineering Department, Engineering School, Mie University, Tsu, Japan.   His research interests include PMSM speed sensorless control.

Muneaki Ishida (M'81) obtained a BS, MS, and PhD in Electrical and Electronic Engineering from Nagoya University, Nogoya, Japan in 1975, 1977, and 1980, respectively. From 1980 to 1987, he was a research associate in the Department of Electrical Engineering, Nagoya University. Since 1987, he has been affiliated with Mie University, Mie, Japan, initially as an associate professor and as a professor since October 1996. He is engaged in research on power electronics, AC motor control system, and matrix converters.

Naoki Yamamura was born in Mie, Japan on October 20, 1964. He obtained a BS, MS, and Dr. Eng. In Electrical Engineering from the Nagoya Institute of Technology in 1989, 1991, and 1993, respectively. Since 1993, he has been associated with the Department of Electrical Intelligence Engineering, Nagoya Institute of Technology. Since 1998, he has been associated with the Department of Electrical and Electronic Engineering, Mie University, where he has been an assistant professor since 1998 and assosiate proffesor since 2008. His present research is the development of power generation systems using natural energy, active filters, and fuel-cell generation systems. He is a member of the IEEE, JIPE, and IEE of Japan.

Kazuhiro Yubai obtained a BE, ME and PhD in Electrical Engineering from Nagoya University, Nagoya, Japan, in 1996, 1998, and 2000, respectively. Since April 2000, he has been with the Department of Electrical and Electronic Engineering, Mie University, Tsu, Japan, where he is currently an associate professor. In 2013, he was a visiting scholar of École Polytechnique Fédérale de Lausanne (EPFL). His research interests include robust control, data-driven control, and motion control.

Satoshi Komada received a BE, ME, and PhD in Electrical Engineering from Keio University, Yokohama, Japan, in 1987, 1989, and 1994, respectively. Since 1989, he has been with Mie University, Tsu, Japan, where he is a professor of electrical and electronic engineering. His research interests include robotics, motion control, muscular strength measurement, and strengthen training, among others.